Journal of Materiomics 11 (2025) 100939

Contents lists available at ScienceDirect

Journal of Materiomics

journal homepage: www.journals.elsevier.com/journal-of-materiomics/

Research paper

Influence of electrode contact arrangements on Polarisation-Electric field measurements of ferroelectric ceramics: A case study of $BaTiO_3$

Erin L. Carroll [a], James H. Killeen [a], Antonio Feteira [b], Julian S. Dean [a], Derek C. Sinclair [a, *]

[a] Department of Materials Science and Engineering, Sir Robert Hadfield Building, University of Sheffield, Mappin Street, Sheffield, S1 3JD, United Kingdom
[b] Materials and Engineering Research Institute, Sheffield Hallam University, Sheffield, S1 1WB, United Kingdom

ARTICLE INFO

Article history:
Received 1 May 2024
Received in revised form
3 August 2024
Accepted 13 August 2024
Available online 15 September 2024

ABSTRACT

A range of partial top full bottom electrodes are used to explore the use of bi-polar Polarisation-Electric field (P–E) measurements to quantify recoverable energy (W_{rec}), energy loss (W_{loss}) and the efficiency (η) of ferroelectric $BaTiO_3$ ceramics. The values obtained are dependent on the ratio of sample thickness (S) and top contact radius (r). With increasing S/r from 0.17 to 1.96 the P–E responses become increasingly distorted and broader. Measurements show W_{rec} increases by a factor of ~1.4 but W_{loss} increases by a factor of ~7 with η decreasing from ~29% to 8%. Finite element modelling was used to simulate the experimental set-up of the sample/electrode arrangements using the Jiles-Atherton model to replicate the ferroelectric behaviour of $BaTiO_3$. These models demonstrate the experimentally applied electric field using a simple geometric correction for sample thickness is an underestimation of the actual field experienced by the material under the top contact at high S/r values. We stress the importance of reporting the contact sizes and thicknesses of samples when using P–E measurements to assess W_{rec}, W_{loss} and η in non-linear dielectric materials. This will allow a fairer comparison of performances between various types of materials being considered for high-energy-density ceramic capacitors.

1. Introduction

The demonstration of Polarisation-Electric field (P–E) hysteresis loops has been used since 1930 to identify ferroelectric materials and establish parameters such as remanent and saturated polarisation, P_r and P_s, respectively along with the coercive field, E_c, Fig. 1. In many cases, for high permittivity (non-conducting) ferroelectrics, the polarisation P at a given time is very nearly equal to the electric displacement, D; however, a small correction is needed for the dielectric displacement to give accurate results for low permittivity dielectrics *via* Equation (1),

$$D(t) = \varepsilon_0 E(t) + P(t) \qquad \text{Equation(1)}$$

where ε_0 is the permittivity of free space, E is the electric field and t is the time. This leads to D and P being interchangeable, and as such many ferroelectricians refer to their measurements as P–E loops. This holds true if the polarisation of the material is given by

$$P = \frac{Q}{2A} = \frac{\int I dt}{2A} \qquad \text{Equation(2)}$$

where Q is the total switched charge over the area A of the electrodes on the sample (assuming the two contacts are of identical area), related to the total integrated current I, which is generated by the ferroelectric domain switching. However, this assumption and measurement pose significant issues for electrically leaky materials and can lead to ambiguity, either as an erroneous diagnosis of ferroelectricity in a non-ferroelectric material or inconclusive evidence for ferroelectricity. If the material has significant conduction (*i.e.* a leaky-dielectric) then the measured current, and as such, charge requires an additional term that is related to the electrical conductivity, σ, of the material and the electric field given by

$$Q = 2PA + \sigma EAt \qquad \text{Equation(3)}$$

The assumption that D and P are directly interchangeable no longer holds. Therefore, if the conductivity of the material is high or becomes high during the measurements (for example under high electric fields), the polarisation due to domain switching will be

* Corresponding author.
E-mail address: d.c.sinclair@sheffield.ac.uk (D.C. Sinclair).
Peer review under responsibility of The Chinese Ceramic Society.

https://doi.org/10.1016/j.jmat.2024.100939

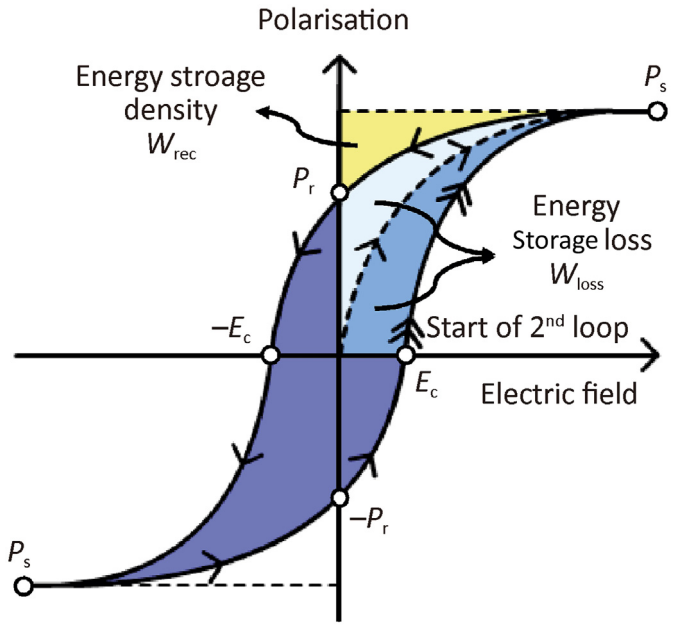

Fig. 1. A schematic representation of an 'ideal' *P*–*E* loop measurements highlighting the polarisation saturation (P_s), remanence (P_r) and coercive field E_c for a typical (non-conducting) ferroelectric material. Based on the upper right quadrant of the *P*–*E* loop, the yellow region shows the energy storage density W_{rec}, the light blue region shows the energy storage loss, W_{loss} for unipolar measurements, and the sum of the light and medium blue regions show W_{loss} for bipolar measurements. Arrows indicate measurement direction, with double arrows showing the start of the second loop.

swamped in a signal that now includes contributions from the electrical conductivity (and the dielectric displacement) with 'cigar'-like loops produced. This is well documented in standard textbooks [1] and, more famously in the article 'Ferroelectrics go bananas' [2]. As much of the current literature ignores this when presenting their data, for present (illustrative) purposes we shall also refer to our data as *P*–*E* loops.

With the recent interest in the development of high energy density and high-efficiency dielectric capacitors for power electronics [3–6], *P*–*E* loop measurements are increasingly being used to quantify energy storage density, $W_{rec,}$ and energy loss density, W_{loss}, to provide an overall efficiency of the capacitor, η, where $\eta = W_{rec}/(W_{rec} + W_{loss})$, Fig. 1 [7–10]. Additionally, these materials need to operate at higher temperatures (*e.g.* 200–300 °C) and electric fields (*e.g.* > 200 kV/cm), thus requiring high breakdown strength. *P*–*E* testing therefore requires high electric fields to be generated and arcing effects between the electrodes to be minimised. Based on a top-bottom electrode arrangement, users typically measure thin samples (recall E = applied voltage/distance of electrode separation) and/or electrode configurations that are not full top-bottom (FTB) but partial (micro) top-full bottom (mTFB) or symmetrical micro-top, micro-bottom in attempts to overcome these issues.

There are several methods based on various measured quantities (in brackets) to establish electric-field induced polarisation, for example, Sawyer-Tower (charge), current step (voltage) and virtual ground (current) [11]. In all cases, the principle is based on quantifying the switched charge, Q, against an applied voltage, V_{app}, at a certain frequency. Users are required to input the area, A, of the electrodes, usually in units of cm^2, to convert Q (C) into P (usually plotted as $\mu C/cm^2$) along with the distance of electrode separation, S (usually in units of cm or m) to convert V_{app} (V) into E (usually plotted as kV/cm or MV/m). For FTB electrodes conversion of Q to P and V_{app} to E is trivial as A and S are easily identified and E across the material (assuming its ideal and electrically homogeneous and isotropic) is uniform. Challenges arise when the two electrodes are of different size and therefore area. What should the user input for the radius of the electrode to calculate A: the reduced radius of the top electrode, an average of the two electrodes or the radius of the full bottom electrode? Furthermore, E across any ideal material now becomes non-uniform. These issues influence the values obtained for W_{rec}, W_{loss} and η. This has been exemplified by Zhang *et al.* [12] who measured the same $NaNbO_3$-based material under FTB and mTFB electrode arrangements using the same instrument but obtained different *P*–*E* loop responses. This resulted in W_{rec} increasing by a factor of ~2 and an increase in η from 33 (FTB configuration) to 47% (mTFB configuration) compared to a FTB arrangement. This highlights the need to consider metrology when testing and characterising dielectric materials for high energy density and high-efficiency ceramic capacitor applications using *P*–*E* measurements.

The simplest scenario in any electrical measurement uses fully terminated top and bottom surface (FTB) electrodes on an ideal linear dielectric that obeys Ohm's law at low electric fields, as shown in Fig. 2a. This gives rise to a uniform flow of current between the contacts based on a material with uniform permittivity, ε, and conductivity, σ. The measured resistance R (Ω) can be converted to σ (usually S/cm) using Equation (4)

$$R = \frac{1}{\sigma}\frac{S}{A} \qquad \text{Equation(4)}$$

where the ratio S/A is known as the geometric correction factor based on the separation (S) and the area of the electrode. The electric field can be written as

$$E = \frac{V_{app}}{S} = \frac{1}{\sigma}\frac{I_{app}}{A} \qquad \text{Equation(5)}$$

where V_{app} and I_{app} are the applied voltage and drawn current on or through the electrode, respectively.

Low-field measurements on ceramics using Impedance Spectroscopy are typically made with fully contacted samples; however, to reach the higher fields required to measure some of the best-performing energy density materials using *P-E* measurements requires >200 kV/cm. This is where micro-contacts based on mTFB and thin samples of various dimensions are employed, Fig. 2b–f and various scenarios associated with charge storage and current flow occur.

When a micro-contact is used in electrical measurements it is no longer a system with simple linear flow. As the top contact is smaller than the bottom, the current can spread out to reduce the resistance by increasing the area over which it is acting, as shown in Fig. 2b.

If a circular contact is assumed to be on a large sheet of homogenous isotropic material with space to spread out unimpeded as depicted in Fig. 2c the spreading resistance can be calculated as

$$R = \frac{1}{\sigma}\frac{1}{4r_{mc}} \qquad \text{Equation(6)}$$

where r_{mc} is the micro-contact radius. Fleig and Maier [13] have shown that the region of high current density (75% of the total current density), which dominates the electrical response, is within a hemispherical volume that extends a distance of approximately $4r_{mc}$ from the surface of the contact. Hence, the geometric factor (Eqn. (4)) is not associated with the thickness of the sample but inversely proportional to four times the micro-contact radius. This is shown schematically in Fig. 2c as the dark blue region under the micro-contact. In many experimental configurations, however, this

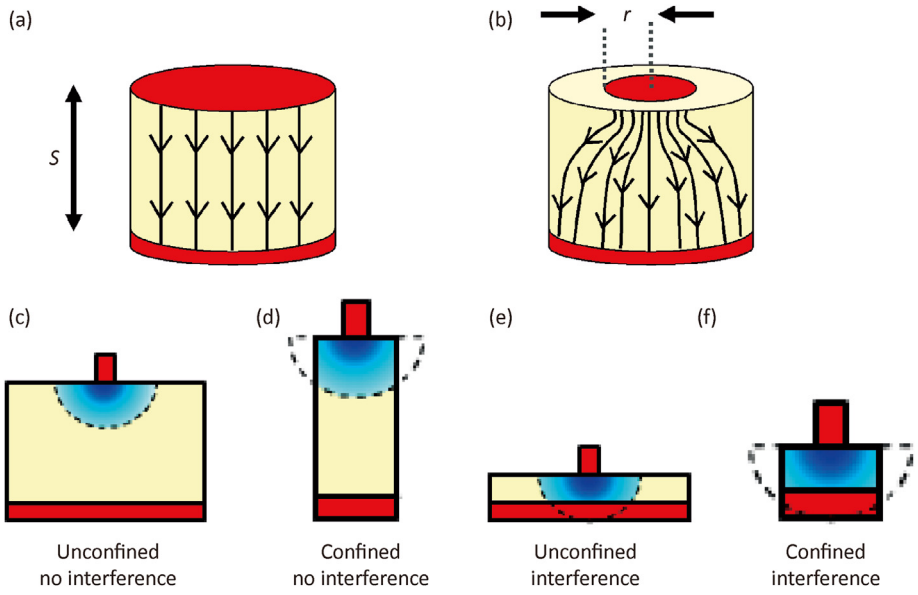

Fig. 2. Schematic representations of current flow and electric field effects in various electrode contact measurements of a system with thickness *S*. (a) Full top-bottom (FTB) contacts where the current flows between the electrodes in a uniform manner. (b) A micro-contact of radius r with a full bottom contact, mTFB. Here the current and field spread outwards from the micro contact. The size of the contact compared to the dimensions of the sample can give rise to various scenarios (c–f) where the current and field can be confined and cause interference between the electrodes. The blue regions under the electrodes are of high current density or electric field.

ideal scenario of unimpeded spreading resistance is not present and various forms of geometrical confinement occur that can give rise to current confinement and/or interference effects [14], Fig. 2d–2f along with other effects such as hindrance arising from voids and cracks [15].

If the sample is relatively thick but the micro-contact is large with respect to the sample surface area, the spreading current is close to the external surfaces, as in Fig. 2d. The current can no longer spread out freely but is confined and therefore increases the measured resistance. If the micro-contact is small and the sample is thin, confinement is not an issue; however, the high current density envelope under the micro-contact now begins to overlap with the lower electrical contact, leading to current interference and a decrease in the measured resistance, Fig. 2e. Interference and confinement effects can occur in the same system as shown in Fig. 2f. In some scenarios, they are beneficial and act to counter-balance each other to produce near-accurate R values for σ. However, this requires precise geometries and in many cases, interference and/or confinement effects introduce significant errors when using mTFB electrode arrangements [14] to establish the σ of a material. The ratio of the sample thickness against the micro-contact radius, S/r, provides a useful metric to indicate the level electrical interference that may be present.

Current density, J, and electric field are linked through the conductivity of the material (assuming Ohmic behaviour, *i.e.* $J = \sigma E$) and therefore the spreading of the current leads to a spreading and localisation of the electric field. The electric field a material experiences under the electrical contact can therefore be significantly different to that assumed by Equation (5). To study the significance of this we combine an experimental and modelling approach on the classic ferroelectric material $BaTiO_3$ to investigate how S/r can affect P–E measurements performed under high electric fields and therefore influence the extracted values of W_{rec} and W_{loss} and consequently η.

2. Experimental section

Undoped $BaTiO_3$ ceramics were fabricated using a commercially available $BaTiO_3$ powder with an average particle size of 200 nm. Green pellets were pressed using a uniaxial press followed by isostatic cold pressing and sintered in air at 1350 °C for 5 h. The resulting ceramics were polished using SiC abrasive paper with isopropanol as a lubricant to ensure the desired thickness of the ceramics. To generate micro-contacts (top) with r between ~ 0.50 mm and 2.00 mm, laser-cut stencils of different radii were used. The top electrode (one per sample) was formed using Au paste, which was heated at 200 °C for 5 min. The full bottom electrode was also applied using Au paste and ceramics with mTFB electrodes were heated to 850 °C for 2 h to harden the Au electrodes. The final diameter of the samples was ~7.7–7.8 mm and a range of thickness (S between ~ 0.3 mm and 1.0 mm) and contact sizes used to produce S/r ratios between 0.17 and 1.96, see supporting information Table SI1.

P–E loops of mTFB electrode ceramics heated to 30 °C and measured at 1 Hz were obtained using a TF Analyzer 2000E with an FE-Module and aixPlorer Software. 30 °C was selected to avoid the orthorhombic to tetragonal crystallographic transition in undoped $BaTiO_3$ at ~22 °C. Multiple bipolar P–E loops were collected at intervals between E_{app} of 5 kV/cm to 20 kV/cm with samples being introduced to higher E_{app} on successive measurements between the minimum and maximum E_{app}.

3. Results and discussion

Laboratory X-ray Diffraction (XRD) confirmed the ceramics to be single-phase and the patterns fully indexed on a tetragonal unit cell. The ceramic microstructure consisted of grains that typically ranged from ~50 μm to 100 μm in size, with some smaller grains of ~20 μm, Supporting Information Fig. SI1. This type of grain structure, ranging from ~70 μm to 100 μm has been reported for other undoped $BaTiO_3$ ceramics sintered at a temperature of 1350/1355 °C [16–18]. The SEM images also revealed a low density of pores (the black spots), ~4 μm in size and typically at the triple points of the grains. The measured density of the ceramics was ~5.99 g/cm^3, yielding an overall density of 99.3% compared to the theoretical density of undoped $BaTiO_3$ (6.03 g/cm^3 [19]). The SEM

images and measured densities confirm the microstructures obtained from these ceramics to be consistent with those reported from other studies on undoped $BaTiO_3$ using similar processing temperature/time profiles and their suitability for *P*–*E* testing.

A typical FTB bipolar P-E loop using an electric field of 20 kV/cm calculated and set using Equation (5) is shown in Fig. 3a (black line) with values of P_{max}, P_r and E_c of ~19.4 μC/cm^2, 11.0 μC/cm^2 and 1.5 kV/cm, respectively. The polarisation values compare well with the range of literature values reported for undoped $BaTiO_3$ sintered at 1350 °C (~16 μC/cm^2 to 22 μC/cm^2) and for those of $BaTiO_3$ ceramics with grain sizes from ~68 μm to 92 μm [20,21]. The coercive fields also match well with reported ranges (~1.5–2.0 kV/cm) for similar ceramics sintered at 1350 °C.

The effects of changing the top contact to a partially covered micro-contact to form mTFB electrodes are shown for the *P*–*E* measurements in Fig. 3a. The apparent polarisation of the material (*i.e.* P_{max} and P_r) increases with increasing *S*/*r* ratio compared to the FTB values despite the electric field reaching the same maximum value of 20 kV/cm in all cases, Fig. 3b and c. The largest *S*/*r* yields the highest P_{max} of ~70 μC/cm^2, Fig. 3b, which is ~3.5 that for the FTB electrode configuration (P_{max} ~ 19.4 μC/cm^2). Similar trends are observed for P_r shown in Fig. 3c. With increasing *S*/*r*, the P-E loops become distorted and broader, especially for $S/r = 1.96$, where it is asymmetric with E_c rising from ~1.5 kV/cm (FTFB) to > 7 kV/cm, also shown in Fig. 3c.

The distortion and broadening of the P-E loops are also observed in the current-field (*I*–*E*) measurements. For FTB, Fig. 3d, there is a clear, well-defined peak increasing to ~900 μA at the coercive field. As the current is low compared to this peak current, this indicates domain switching is the dominate contributor in the *P*–*E* response compared to the contributions from the conductivity or permittivity-electric field dependencies [22]. This provides a justification that the data can be referred to as a *P*–*E* loop; however, the *I*–*E* profile becomes significantly modified as the *S*/*r* ratio increases. The peak height reduces to ~5 μA for $S/r = 1.96$ and is less well defined and broader as shown in Fig. 3e. Such a decrease in peak height and broadening has been shown to occur if there is a rise in the sample temperature in doped $BaTiO_3$ ceramics [22]. In this case, the conductivity of the sample is becoming a dominant component in the signal and as such there is low justification for referring to this as a *P*–*E* loop and really should be reported as a *D*–*E* response. It should be noted, that there also exists an asymmetry in this peak which could be linked to the contact radius and field direction.

Table 1
Recoverable energy (W_{rec}) and energy loss (W_{loss}) with associated efficiencies η for $BaTiO_3$ ceramics with various mTFB *S*/*r* electrode arrangements measured from bipolar measurements. Values for full top and bottom electroded samples (FTB) are included for comparison.

S/*r*	W_{rec} (J/cm^3)	W_{loss} (J/cm^3)	Efficiency, η
FTB	0.0532	0.0622	46.1
0.17	0.0502	0.125	28.7
0.25	0.0503	0.127	28.4
0.47	0.0548	0.161	25.3
0.77	0.0556	0.259	17.7
0.81	0.0456	0.393	10.4
0.97	0.0476	0.466	9.26
1.23	0.0579	0.563	9.32
1.96	0.0720	0.890	7.49

S/*r* has a strong influence on the energy storage density. This is shown both in Table 1 for W_{rec} and W_{loss}, with the efficiencies for the respective *P*–*E* loop measurement also shown in Fig. 3f. It is worth stressing that the FTB configuration for these $BaTiO_3$ ceramics always provides the highest efficiency (~46%) compared to the mTFB electrodes, Table 1. For FTB and $S/r < 1$, W_{rec} is reasonably consistent until a value of $S/r = 1.96$, however, it is W_{loss} that increases throughout this range by over 14 times. This increase can be attributed to the change in the *P*–*E* loop due to the increased conductivity contribution in the measurement. As such the loop becomes distorted and loses its defined switching behaviour that is observed at FTB or lower *S*/*r* ratios, Fig. 3a. This increase in W_{loss}

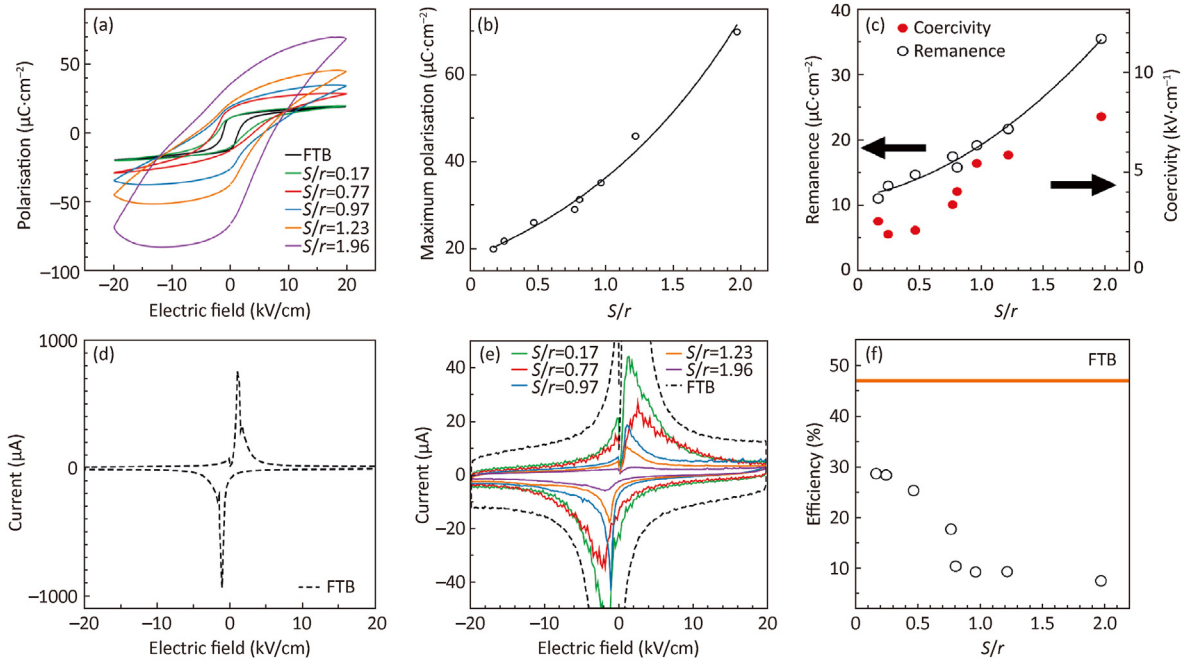

Fig. 3. (a) Experimental *P*–*E* loops of $BaTiO_3$ ceramics for various *S*/*r* ratios using the bipolar measurements. (b) the associated P_{max}. (c) P_r (open symbols, left axis) and E_c (full red symbols, right axis) *versus* *S*/*r*. A guide to the eye is overlaid in both (b) and (c) to show the trend for P_{max} and P_r, respectively. (d) *I*–*E* plots for a FTB system and (e) for the full *S*/*r* data set. (f) The calculated efficiency, η, *versus* *S*/*r*. The FTB contact configuration is overlaid as a comparison using an orange line.

from 0.062 J/cm^3 to 0.890 J/cm^3 over the S/r range dramatically decreases the measured efficiency from η ~46.1%–7.5%.

3.1. Design and analysis of computational model

To determine if the effects observed can be linked to the spreading of the electric current associated with the micro-contact, finite element (FE) modelling using COMSOL multi-physics was employed to simulate the experimental analysis procedure [23]. A computational model was constructed as a rectangle of width 3.85 mm, with a thickness set using Table SI1. This was then axially revolved around its edge to create a disc of diameter 7.7 mm. Electrical boundary conditions were set along the lower surface to create a ground contact. The full or micro contact was then assigned to the top of the disc with a triangular (1 Hz) voltage applied, mimicking the experimental setup. The maximum V_{app} was scaled using the sample thickness (Equation (5)) as shown in Fig. 4a to generate $E_{app} = 20$ kV/cm through the sample. All other boundaries were set to be electrically insulating. The thicknesses of $S = 0.33$ mm used in the case of $S/r = 0.17$ required $V_{app} = 660$ V to generate the desired $E_{app} = 20$ kV/cm, whereas for $S/r = 0.81$ with a thickness of $S = 1.01$ mm a higher $V_{app} = 2020$ V was required to generate the equivalent E_{app}, Fig. 4a.

The Jiles-Atherton model [24–26] was used to simulate the ferroelectric behaviour of undoped $BaTiO_3$ (see SI for more details). This model allows the simulation of a ferroelectric material by assuming the total polarisation can be represented as a sum of reversible and irreversible parts. The properties required to describe the ferroelectric behaviour are saturation polarisation, domain wall density, inter-domain coupling, polarisation reversibility and pinning loss. These values were fitted by implementing an iterative regression analysis-based approach (least squares fitting) on the FTB experimentally determined data set. The resulting model parameters are shown in the Supplementary information, Table SI2. The simulation of the FTB model in Fig. 4b in red, compares well against the experimental data shown in black. Note that the analytical model developed here is not set up to exactly match the experimental data but to provide a controlled simulated P-E loop that can be subjected to changes in the S/r ratio and the associated changes or trends recorded and observed. The fitted parameters are maintained through all simulations presented here to provide a demonstration of how the material should respond with changes only in the S/r ratio and not through any additional losses, such as heating effects, which may occur experimentally.

Simulations were then performed for the range of S/r given in Table SI1 and plots of the polarisation experienced at the micro-contact versus the electric field were calculated from Equation (5) and are shown in Fig. 4c. Slim loops were obtained from the simulations with P_{max} increasing from ~21 μC/cm^2 to 28 μC/cm^2 but E_c decreasing from 2.25 kV/cm to 0.63 kV/cm as S/r increases from 0.17 to 1.96, respectively. A comparison of the experimental data versus the simulated data for the FTB and various S/r values is given in Fig. SI2. It is clear there is good agreement for FTB and $S/r = 0.17$, Fig. SI2a–2b, respectively but significant deviations occur for the larger S/r values of 0.97 and 1.96, Fig. SI2c–2d, respectively.

A cross-sectional view of the electric field at maximum V_{app} experienced by the material for various S/r ratios is shown in Fig. 4d and the electric field profile over the sample surface is highlighted in Fig. 4e and through the depth of the sample in Fig. 4f. The black line in Fig. 4d shows the length of the top micro contact in each case and for all three figures, the electric field is plotted on a log scale to show the large changes obtained.

For $S/r = 0.17$, the electric field generated for the majority of the contact surface area is 10 kV/cm, half of the assumed 20 kV/cm. Although this does rise to over 150 kV/cm at the edges of the contact, the integrated average electric field over the contact is 17 kV/cm, still below the value assumed in Fig. 4d and Fig. 4e. On

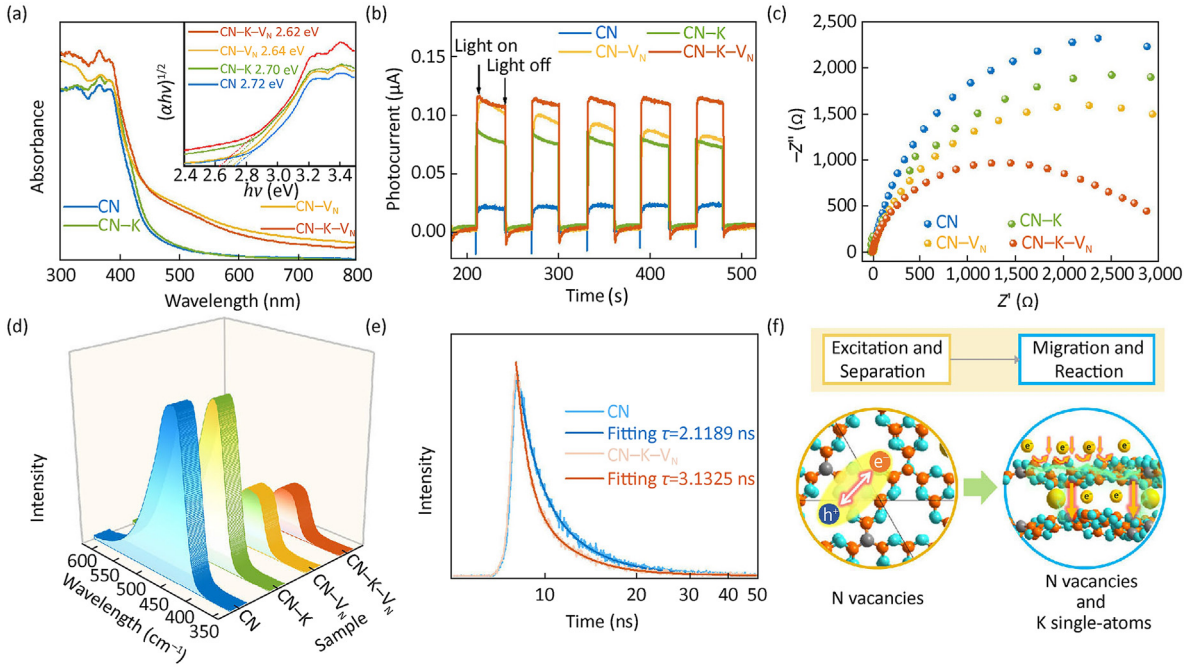

Fig. 4. Simulation of P–E loops using finite element modelling. (a) To be consistent with experiments the applied voltage, V_{app}, is scaled to thickness as shown for $S/r = 0.17$ and 0.81. (b) An FTB experimentally determined P–E loop compared directly to the FE model using the Jiles-Atherton method [22–24]. (c) Simulated P–E loops for various S/r plotted versus the assumed electric field. (d) Cross-sections of the localised electric field experienced in the material for three S/r values where (e) shows the local electric field generated from the centre of the contact across the surface of the sample and (f) shows the electric field along the depth of the sample at the centre of the contact.

increasing S/r to 0.97 the field under the contact increases to 27 kV/cm due to the smaller size of the contact and it steadily rises to over 560 kV/cm at the edges, Fig. 4d and Fig. 4e. This leads to an integrated average of 92 kV/cm over the entire contact surface. As S/r is further increased, the contact average dramatically rises to 229 kV/cm for $S/r = 1.96$, a factor of 11 higher than the assumed field. This can be attributed to the small size of the contact where the high concentration of field at the edges now increases the electric field experienced at the centre and edges of the contact to 99 kV/cm and 650 kV/cm, respectively as shown in Fig. 4d and Fig. 4e.

In all these cases, electrical confinement is not significant as the electric field at the external surface is as low as 1 V/cm, Fig. 4d. For low S/r ratios; however, there is visible electrode-to-electrode interference. For example, for $S/r = 0.17$, the high field envelope encompasses the lower electrode, shown by the flat response in Fig. 4f and this causes the resistance to decrease. As the contact is relatively wide, the edge effects from the contact do not interfere with the field at the centre and the field is uniform and extends across the contact surface relatively unchanged, Fig. 4e. As the thickness of the sample increases the high field envelope rises above the lower contact ($S/r = 0.97$) and moves to a lower interference configuration as shown by the drop in electric field in Fig. 4f. This creates greater current spreading and a higher, more localised, non-linear electric field to be present directly under the contact.

Extracting W_{rec} and W_{loss} from the simulated data in Fig. 4 (shown in Table 2) highlights that the efficiency increases with S/r from 34.7% when simulating an FTB arrangement to 42.8% for $S/r = 1.23$. This increase, in contrast to the decrease observed experimentally, can be attributed to the large fields and more localised current under the contact which causes a greater proportion of saturated material in the measurement. These differences arise due to our simulations maintaining the fitted Jiles-Atherton model from the FTB data and assuming that the intrinsic material properties remain unchanged throughout the measurements, which is unlikely to be true [22].

3.2. Comparison of experimental results and computational model

These models demonstrate that the experimentally applied electric field calculated by Equation (5) is an underestimate of the actual field the material is experiencing under the top contact. To determine the strength of this field we can use these simulations to integrate the electric field over the micro-contact. This is shown as a function of S/r in Fig. 5a. There is a strong, non-linear rise in the field strength with increasing S/r. These electric fields are now used as scaling factors for both simulation and experimental data. As an example, for $S/r = 1.96$ the integrated electric field is 229 kV/cm compared to the assumed applied value of 20 kV/cm, generating a scaling factor of 11.5. Employing these factors, the electric field in the modelled data can be rescaled as shown in Fig. 4c, where now the *P-E* loops overlay with similar E_c ~2.25 kV/cm values, Fig. 5b and c. This highlights, when rescaled, the FTB and low S/r ratios are now minor loops of the larger S/r ratios as would be expected.

These same factors can also be applied directly to the experimental data in Fig. 3a and rescaled plots are shown in Fig. 5d. As shown, similar to the rescaled modelling data in Fig. 5b the *P–E* loops now start to nest, in Fig. 5d. While the simulated *P–E* loops match well with FTB and low S/r ratios, as S/r increases, significant deviations in the loop shape are observed (see SI and Fig. SI2) with the experimental data starting to clearly resemble the 'cigar-shaped' loops referred to in Ref. [2] due to the presence of additional losses. We note that although W_{rec} and W_{loss} alter due to the rescaling, as shown in Table 3, η remains the same as that shown in Table 1 and Fig. 3d due to the scaling cancelling in the efficiency calculation.

For low S/r ratios, the *P–E* loops follow a very similar profile, maintaining a slimmer shape and relatively high efficiency is obtained. As the S/r ratio rises above unity, the *P–E* loops become broader, indicating greater energy loss, Fig. 5d and Table 3. As before for $S/r = 1.96$, the *P–E* loop is distorted with a large enclosed area and a significant increase in W_{loss} to over 10 J/cm^3, Table 3. The rescaled values for the electric field at this S/r ratio are extremely high, rising to over 200 kV/cm. The coercivity values obtained from the rescaled bipolar *P–E* data in Fig. 5d versus S/r are shown in Fig. 5e. For S/r below ~0.5, the slim *P–E* loops with a well-defined saturated shape have a coercivity of <4 kV/cm but it then rises steeply to >80 kV/cm as the *P–E* loops lose their saturated shape and become larger with greater loss. At low S/r the loops again nest well. As the S/r ratio increases towards 1, the loops again become broader, indicating higher loss and lower efficiency, as shown in Table 3.

3.3. Discussion

The experimental and simulated *P–E* results presented here show how relatively small changes in the electrode size and/or thickness of a sample can result in significant variability in the extracted material values for W_{rec} and especially W_{loss} *via P–E* loop measurements. This discrepancy is driven by the variability of the electric field the material experiences under the partial contact, which is induced by changes in the S/r ratio. For low S/r ratios, the electric fields are typically uniform and match those estimated by Equation (5). This is also observed in the sharper peaks in the *I–E* plots indicating domain switching dominating the response with little contribution from conductivity and the dielectric displacement. At higher S/r ratios, electric fields exceeding 600 kV/cm can be generated near the edge of the contacts, whereas they are below 100 kV/cm in the centre of the contact. This local electric field generates variations in the integrated current inducing additional contributions in the signal. As such, the *P-E* loops become distorted, and the loss increases as the domain switching current is increasingly swamped in a signal that contains other contributions. It is clear from this, that the size of the contact and thickness of the sample play significant roles. For example, in our experiments, samples with $S/r = 0.47$ and 1.23 only differ in thickness by 0.04 mm (0.94 mm *vs.* 0.98 mm) but due to the contact size reducing from 2.0 mm to 0.5 mm, the efficiency of the material was more than halved decreasing from ~25.3% to 9.3%.

Although many research groups create contacts of the same size on their samples (*e.g. via* masks for microcontacts), the thickness of the samples (and therefore S/r) may vary and this can play a significant role. In particular, the thickness is used to calibrate the applied voltage using Equation (2) and our results show that it plays a key role in how the current spreads out from the micro-contact, and as such, the electric field distribution. For example, in the experimentally measured cases of $S/r = 0.77$ and 1.96, both

Table 2
Recoverable energy (W_{rec}) and energy loss (W_{loss}) with associated efficiencies η for the simulated results as shown in Fig. 4.

S/r	W_{rec} (J/cm^3)	W_{loss} (J/cm^3)	Efficiency, η
FTB	0.0419	0.0788	34.7
0.17	0.0830	0.1450	36.4
0.77	0.1170	0.1880	38.3
0.97	0.1770	0.2720	39.4
1.23	0.1780	0.2380	42.8
1.96	0.1760	0.2400	42.3

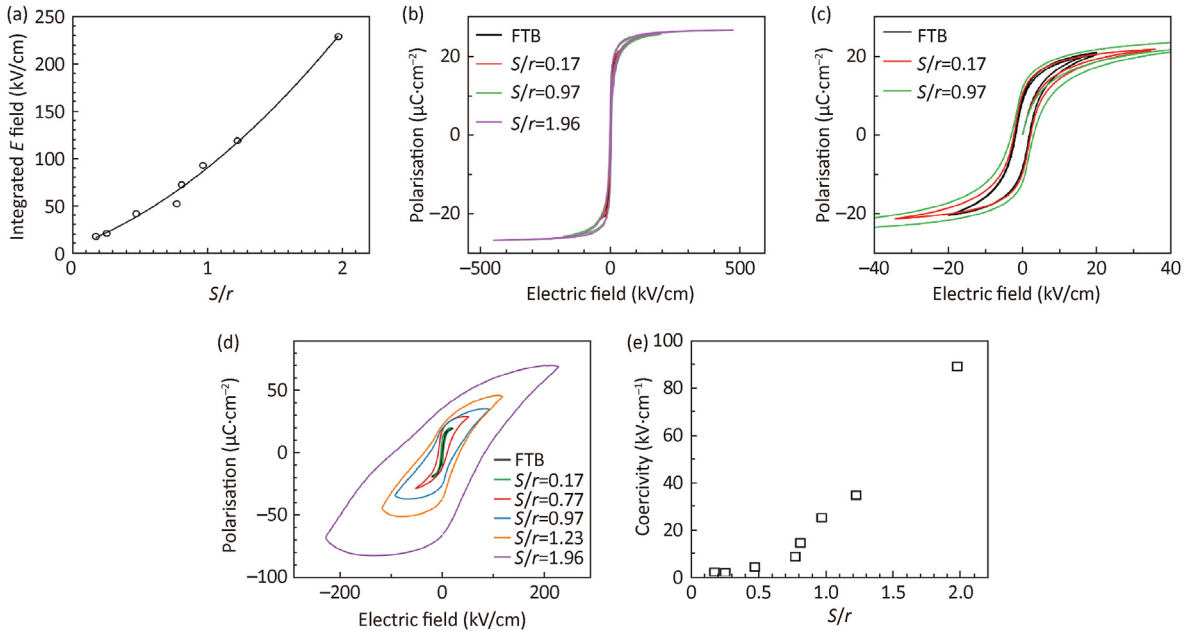

Fig. 5. (a) Integrated electric field on the micro-contacts for a range of *S*/*r* ratios. (b) Rescaled *P*–*E* loops of the modelled data shown in Fig. 4c with FTB and lower *S*/*r* ratios shown in (c) for clarity. (d) Experimental data from Fig. 3a replotted using the integrated fields. At low *S*/*r* the *P*–*E* loops nest but with increasing *S*/*r* increasing distortion of the loops becomes more evident. (e) Coercivity after rescaling the measurements versus *S*/*r*.

Table 3
Rescaled recoverable energy (W_{rec}) and energy loss (W_{loss}) of the *P*–*E* loops with associated efficiency, η as a function of the *S*/*r* ratio.

S/*r*	Scale factor	W_{rec} (J/cm^3)	W_{loss} (J/cm^3)	Efficiency, η
FTB	1.000	0.0532	0.0622	46.10
0.17	0.870	0.0437	0.1090	28.70
0.25	1.030	0.0518	0.1310	28.40
0.47	2.070	0.1140	0.3340	25.30
0.77	2.600	0.1450	0.6720	17.70
0.81	3.610	0.1640	1.4200	10.40
0.97	4.630	0.2200	2.1600	9.26
1.23	5.940	0.3440	3.3400	9.32
1.96	11.500	0.8250	10.2000	7.49

possess the same micro-contact radius but their thickness differs by 0.59 mm (0.39–0.98 mm, respectively). This thicker sample causes the electric field to be strongly localised under the contact, broadening the loop and substantially increasing the loss. This results in the efficiency of the sample decreasing from ~17.7% to 7.5%.

As shown by Fig. 5 and the efficiencies generated from the corrected data, there are still other phenomena reducing reliability. At low *S*/*r* ratios, the *P*–*E* loops overlay and only small changes in efficiency are measured. As *S*/*r* increases, the electric field localises and a broadening in the *P*-*E* loop is observed experimentally with associated changes in the *I*–*E* plots. This distorted loop shape, which resembles the 'cigar-shaped' loops referred to in Ref. [2] is not seen through the modelled data and as such is arising from other factors associated with high fields, such as defect movement, irreversible domain movement, leakage in the form of conductivity and/or joule heating. As noted in Ref. [2], there can be significant contributions to switched charge as highlighted in Equation (3). The asymmetry observed in the *I*–*E* plots also indicates the frequency and direction of the field sweep could play a significant role in the loop shape. All these additional contributions illustrate that what is being measured is actually a *D*–*E* loop which should not be assumed to represent the *P*–*E* response of the sample. This can only be achieved with appropriate subtractions of the dielectric displacement and conductivity effects which can be challenging to determine. As such, only by using low *S*/*r* ratios with the largest contact size that can be created without leading to arcing would provide the greatest confidence in such measurements and in the assumption that it represents a *P*–*E* loop response.

The results presented here are for ferroelectric $BaTiO_3$ ceramics where W_{rec} and η increase and decrease, respectively with increasing *S*/*r*. This is in contrast to a related study on $NaNbO_3$-based Anti-Ferro-Electric (AFE) materials where efficiency was reported to increase for a mTFB compared to an FTB arrangement [12]. Furthermore, mechanical self-confinement associated with radial compressive stresses exerted on the micro-top electroded area by the unelectroded portion of AFE $Pb(Zr,Ti)O_3$-based capacitors has been attributed to enhancing energy storage density [26]. This highlights that various trends with *S*/*r* may be observed depending on the type of non-linear dielectric material being investigated.

4. Conclusions

Since the 2008 article 'ferroelectrics go bananas' [2], the estimated number of peer-reviewed research articles referring to "polarisation-electric field loops" has increased from ~300 to over 1400 in 2023, using a simple Google Scholar search. This technique now underpins and helps drive materials discovery/optimisation, especially in the development of efficient high-energy-density ceramic capacitors. Most of the published work indicates how changes in composition or processing affect the material's energy density storage and performance, leading to new avenues of research. In these, however, few refer to their sample geometries and typically, only the applied voltage and assumed electric field based on Equation (2) is reported. In Ref. [2] Scott noted that many articles are "reporting completely meaningless coercive field and

remanent polarisation values extracted from cigar-shaped loops that are typical of lossy dielectrics and have very little to do with the true ferroelectric properties of the material studied". Our work goes further to show that even if saturation is achieved, sample thickness (S) or electrode contact size (r) needs to be discussed to allow correct interpretation and meaningful comparisons to be made.

Here we have used ferroelectric $BaTiO_3$ as a non-linear dielectric and demonstrate the losses and extracted efficiencies from P–E loop measurements to increase and decrease, respectively with increasing S/r. In the literature, however, there are reports of increasing efficiencies based on partial as opposed to full electrode contacts on AFE $NaNbO_3$—and $Pb(Zr,Ti)O_3$-based materials [27]. It is therefore important that the research community that uses P–E type-measurements to report energy storage performance on the wide range of non-linear dielectrics, from ferroelectric, relaxor ferroelectric and AFE materials to consider if they are measuring P or D. The former is associated with ferroelectric domain switching, P; however, the latter contains additional contributions from the dielectric displacement and electrical conductivity, σ of the material. In all cases, however, reporting the contact size and thickness of the samples used for measurements should be made allowing researchers to make better comparisons and gain more confidence and an informed understanding of the observed trends.

CRediT authorship contribution statement

Erin L. Carroll: Writing – review & editing, Writing – original draft, Methodology, Investigation, Formal analysis. **James H. Killeen:** Writing – review & editing, Methodology, Investigation, Data curation. **Antonio Feteira:** Writing – review & editing, Supervision, Resources. **Julian S. Dean:** Writing – review & editing, Writing – original draft, Visualization, Validation, Supervision, Software, Resources, Project administration, Methodology, Investigation, Formal analysis, Data curation. **Derek C. Sinclair:** Writing – review & editing, Writing – original draft, Visualization, Validation, Supervision, Software, Resources, Project administration, Methodology, Investigation, Formal analysis, Data curation, Conceptualization.

Declaration of competing interest

The authors declare they have no known competing financial interests or personal relationships that could have appeared to influence the work reported in this paper.

Acknowledgements

The authors would like to acknowledge the EPSRC funding to support this work through a CASE conversion DTP grant EP/T517835/1.

Appendix A. Supplementary data

Supplementary data to this article can be found online at https://doi.org/10.1016/j.jmat.2024.100939.

References

[1] Lines ME, Glass AM. Principles and applications of ferroelectrics and related materials. Oxford University Press; 1977.
[2] Scott JF, go bananas Ferroelectrics, Phys J. Condens Matter 2008;20:021001.
[3] Hideki O, Randall CA, Trolier-Mckinstry S. High-energy density capacitors utilizing 0.7 $BaTiO_3$-0.3 $BiScO_3$. J Am Ceram Soc 2009;92(8):1719–24.
[4] Qi H, Zuo R, Xie A, Tian A, Fu J, Zhang Y, et al. Ultrahigh energy-storage density in $NaNbO_3$-based lead-free relaxor antiferroelectric ceramics with nanoscale domains. Adv Funct Mater 2019;29(35):1903877.
[5] Pan H, Li F, Zhang Q, Lan S, Zheng Y, Ma J, et al. Ultrahigh–energy density lead-free dielectric films *via* polymorphic nanodomain design. Science 2019;356:578–82.
[6] Wang G, Lu Z, Li Y, Li L, Ji H, Feteira A, et al. Electroceramics for high-energy density capacitors: current status and future perspectives. Chem Rev 2021;121(10):6124–72.
[7] Qi H, Xie A, Tian A, Zuo R. Superior energy-storage capacitors with simultaneously giant energy density and efficiency using nanodomain engineered $BiFeO_3$-$BaTiO_3$-$NaNbO_3$ lead-free bulk ferroelectrics. Adv Energy Mater 2020;10:1903338.
[8] Wang G, Li J, Zhang X, Fan Z, Yang F, Feteira A, et al. Ultrahigh energy storage density lead-free multilayers by controlled electrical homogeneity. Energy Environ Sci 2019;12:582–8.
[9] Qi H, Zuo R. Linear-like lead-free relaxor antiferroelectric $(Bi_{0.5}Na_{0.5})TiO_3$-$NaNbO_3$ with giant energy-storage density/efficiency and super stability against temperature and frequency. J Mater Chem A 2019;7:3971–8.
[10] Wang X, Fan Y, Zhang B, Mostaed A, Li L, Feteira A, et al. High discharge energy density in novel $K_{1/2}Bi_{1/2}TiO_3$-$BiFeO_3$ based relaxor ferroelectrics. J Eur Ceram Soc 2022;42(15):7381–7.
[11] Prume K, Schmitz T, Tiedke S, Waser R, Böttger U, Tiedke S. Polar oxides: properties, characterization, and imaging. J Wiley & Sons; 2004.
[12] Zhang M-H, Fulanovic L, Zhao C, Koruza J. Review on field-induced phase transitions in lead-free $NaNbO_3$-based anitferroelectric oxides for energy storage. J Materiomics 2023;9(1):1–18.
[13] Fleig J, Maier J. Local conductivity measurements on AgCl surfaces using microelectrodes. Solid State Ionics 1996;85:9–15.
[14] Veazey RA, Gandy AS, Sinclair DC, Dean JS. Modeling the influence of two terminal electrode contact geometry and sample dimensions in electro-materials. J Am Ceram Soc 2019;102(6):3609–22.
[15] Ma H, Sinclair DC, Dean JS. A finite element study on the influence of surface cracks on micro-contact impedance spectroscopy measurements. Solid State Ionics 2023;393:116173.
[16] Lee S, Paik U, Hackley VA, Jung Y-G, Yoon K-J. Microstructure and permittivity of sintered $BaTiO_3$: influence of particle surface chemistry in an aqueous medium. Mater Res Bull 2004;39(1):93–102.
[17] Kanata T, Yoshikawa T, Kubota K. Grain-size effects on dielectric phase transition of $BaTiO_3$ ceramics. Solid State Commun 1987;62(11):765–7.
[18] Lee H-Y, Kim J-S, Hwang N-M, Kim D-Y. Effect of sintering temperature on the secondary abnormal grain growth of $BaTiO_3$. J Eur Ceram Soc 2000;20:731–7.
[19] Tsuji K, Ndayishimiye A, Lowum S, Floyd R, Wang K, Wetherington M, et al. Single step densification of high permittivity $BaTiO_3$ ceramics at 300 °C. J Eur Ceram Soc 2020;40(4):1280–4.
[20] Huang Y, Zhao C, Wu B, Zhang X. Grain size effects and structure origin in high performance $BaTiO_3$-based piezoceramics with large grains. J Eur Ceram Soc 2022;42(6):2764–71.
[21] Fujii I, Trolier-McKinstry S. Temperature dependence of dielectric nonlinearity of $BaTiO_3$ ceramics. Microstructures 2023;3:2023045.
[22] Yan H, Inam F, Viola G, Ning H, Zhang H, Jiang Q, et al. The contribution of electrical conductivity, dielectric permittivity and domain switching in ferroelectric hysteresis loops. J Adv Dielec 2011;1(1):107–18.
[23] COMSOL Multiphysics® v. 6.1. www.comsol.com. COMSOL AB, Stockholm, Sweden.
[24] Jiles DC, Atherton DL. Theory of ferromagnetic hysteresis. J Appl Phys 1984;55(6):2115–20.
[25] Jiles DC, Atherton DL. Theory of ferromagnetic hysteresis. J Magn Magn Mater 1986;61:48–60.
[26] Jiles DC, Thoelke JB, Devine MK. Numerical determination of hysteresis parameters for the modeling of magnetic properties using the theory of ferromagnetic hysteresis. IEEE Trans Magn 1992;28:27–35.
[27] S E Young, J Y Zhang, W Hong and X Tan. Mechanical self-confinement to enhance energy storage density of antiferroelectric capacitors, J Appl Phys 113 [5] 20130054101.

Miss Erin Carroll received her MEng in Material Science and Engineering (research) in 2023 (Sheffield). She is studying her Ph.D. (Faculty award scholarship) on local structure-property relationships in A-site deficient perovskites supervised by Prof. Sinclair, Dr. Dean and Dr. Owen within the Functional Materials Group in the Department of Materials Science and Engineering at the University of Sheffield, UK.

Mr James Killeen received his MEng in Aerospace Engineering in 2020 (Sheffield) and is studying for his Ph.D. on next generation materials for Multi-Layer Ceramic Capacitors which is sponsored by KAVX Ltd and is supervised by Prof. Sinclair and Dr. Dean within the Functional Materials Group in the Department of Materials Science and Engineering at the University of Sheffield, UK.

Professor Antonio Feteira is a Professor in advanced functional oxides for electronic, energy and biomedical applications at Sheffield Hallam University, UK His research focuses on the establishment of composition-structure-property relationships in new advanced functional oxides along with the fabrication of prototype devices *via* 3D integration of these materials.

Dr. Julian Dean is a Senior lecturer in Materials Modelling within the Functional Materials Group in the Department of Materials Science and Engineering at the University of Sheffield, UK. He is recognised for simulating the effects of microstructure and electrical behaviour on both functional oxides and magnetic materials.

Professor Derek Sinclair is a Professor of Materials Chemistry within the Functional Materials Group in the Department of Materials Science and Engineering at the University of Sheffield, UK. He is recognised for his ability to probe the structure (crystal and defect)-composition-microstructure-property relationships in a wide range of functional oxides, spanning from polar dielectrics *via* mixed conductors to solid electrolytes.